Journal Name

ARTICLE TYPE

The Aggregation of Striped Nanoparticles in Mixed Phospholipid Bilayers

Sang Young Noh,[a‡] Anthony Nash,[b‡] and Rebecca Notman[a]

The unique and adjustable properties of nanoparticles present enormous opportunities for their use as targeted drug delivery vectors. For example, nanoparticles functionalized with key surface ligands have been shown to pass through phospholipid bilayers without causing localised disruption. However, the further effects nanoparticles have on multi-component phospholipid bilayers remain unclear. We use coarse-grained computational models to investigate the structural properties of mixed phospholipid bilayers in the presence of ligand-functionalized nanoparticles. Model bilayers are composed of DPPC, DUPC, DFPC and cholesterol, and the nanoparticles are striped with a hydrophobic-ligand band and charged-ligand spherical caps. Our results show that: nanoparticles aggregate near unsaturated phospholipid regions, phospholipid bilayer phase-separation is promoted in the presence of nanoparticles, and the heterogeneous components of a phospholipid bilayer play a significant role in the lateral organization of nanoparticles. This study highlights the need for considering the complexity of realistic phospholipid bilayers when optimising ligand functionalized nanoparticles for efficient drug delivery vectors.

1 Introduction

The development of novel mechanisms for the delivery of drugs to biological cells has been the subject of intense study in recent years[1–6]. For small drug molecules the main barrier to efficient delivery is typically the cell membrane lipids[7,8]. The rate of passive diffusion depends on the concentration gradient between the aqueous exterior and the cell interior[8]. In effect, an excessive injection of drug molecules may be required and it may not yet result in the efficient delivery of drug molecules[8]. In addition to the aforementioned obstacle to drug delivery, membrane proteins can act as barriers to a vast majority of molecules. For example, the membrane protein P-glycoprotein acts as a molecular pump expelling drug molecules from the inter-cellular space to the extent that it has been implicated in multidrug resistance of cancer cells[9].

To overcome these barriers, drug-delivery vectors of various types have been considered. Nano-sized particulates, or nanoparticles (NP), are of increasing interest due to their potential for efficient, targeted drug delivery, due to a high surface-to-volume ratio[10], which allows for strong interactions with the cellular membrane. NPs have demonstrated a level of effectiveness through multiple applications in targeted therapy[5,11,12]. However, there are open questions regarding the physical mechanism of how NPs interact with cell membranes, notably the role of the local diversity in the membrane itself and within the cytoplasm of the cell interior[6,10]. For example, phospholipid molecules affect the assembly of the bilayer due to the varying degrees of saturation of the tailgroups, variations in tail length, and/or changes in headgroup functionality. These characteristics affect the structure and structural phase in the bilayer, with regions ranging from stable yet fluid-like disordered to highly ordered[13–15].

Membrane proteins, sterols and sphingolipid-like molecules are known to change the properties of the local phospholipid composition[16]. For example, an increase in cholesterol is known to reduce the curvature of the membrane[17]. An ideal targeted drug delivery system must be designed to minimise disruption to the membrane, whilst being able to freely traverse the lipid bilayer. Understanding the affect NP composition would have on the local cell environment is essential to achieve this goal.

Ligand-functionalized NPs are of particular interest for drug delivery due to the large variety of pharmacological and surface properties they can exhibit. For example, an NP with an inert gold core can be functionalized with thiolated ligands, which in turn can be functionalized with therapeutic drug molecules such as the chemotherapeutic agent, Paclitaxel[18–21]. Chemically optimized NPs allow the delivery of hydrophilic drug molecules through the hydrophobic region of the phospholipid membrane.[22–24].

The effects of NP ligands on phospholipid arrangement has been the subject of several studies. For example, amphiphilic surface ligands result in spontaneous adsorption of the NP into the bilayer via an initial attraction between the bilayer phospho-

[a] *Department of Chemistry, University of Warwick, Coventry, United Kingdom*
E-mail: s.y.noh@warwick.ac.uk
[b] *Nuffield Department of Clinical Neurosciences, University of Oxford, Oxford, United Kingdom*

† Electronic Supplementary Information (ESI) available: [details of any supplementary information available should be included here]. See DOI: 00.0000/00000000.

‡ These authors contributed equally to this work.

lipid headgroups and the NP surface ligands. This is followed by hydrophobic interactions between the NP surface ligands and bilayer phospholipid tail groups[25,26]. Studies using model membranes have shown how hydrophilic ligand-functionalized NPs are stabilized through a snorkelled configuration, where ligands adjust to maximise the hydrophobic and hydrophilic contacts with the phospholipid environment and the phospholipid-water interface[26]. Katz and Van Lehn demonstrated that the snorkelling process is driven by minimising the exposure of the hydrophobic bilayer regions around the NPs[25,27]. In particular, the higher the rigidity of the functionalized ligands on the NP surface the greater the free energy cost of insertion. Jackson *et al.* found that by using a mixture of charged and hydrophobic NP surface-bound ligands it was possible to design an NP that could translocate the bilayer structure whilst minimising local disruption[28]. Headgroup charge can also affect the insertion mechanism of the NP dramatically as seen from coarse-grained simulations of cationic, hydrophobic and anionic NPs in a mixed-charge bilayer[29]. By increasing the surface charge density of the NP there is an increase in the contact area between the phospholipid headgroups with the charged ligands on the NP surface, followed by the mediation of NP insertion through favourable hydrophobic contacts between the phospholipid tails and the NP ligands.

The effects of ligand-functionalized nanoparticles on the nature of *heterogeneous* phospholipids bilayers are not well understood; this is the focus of the present study. Rigid NPs with hydrophobic surface properties have demonstrated an effect on bilayer phase-separation. For example, Barnoud *et al.* demonstrated using mixtures of aliphatic and aromatic hydrophobic particulates and NPs in mixed DPPC, DUPC and cholesterol bilayers that aliphatic compounds aggregate near the domain interface, while aromatic compounds integrate to the disordered regions and stabilise the phases[30]. The phase-separated nature of a mixed phospholipid bilayer remains contentious, but growing evidence suggests that appropriate NP surface chemistry contributes to bilayer phase separation.

In this work, we use coarse-grained Molecular Dynamics (MD) simulations to explore the effect of striped NPs (S-NP) on the properties of a bilayer composed of a mixture of saturated and unsaturated phospholipids and cholesterol. The S-NP topology was chosen as it has been shown to provide the critical amphiphilic property that can both traverse the hydrophilic solvent/bilayer exterior and the hydrophobic interior[20,31]. Hence, the possibility of aggregation of such NPs in the presence of domain-like structures within the bilayer is greatly increased. Two bilayer mixtures (DPPC-DUPC and DPPC-DFPC) and one monophospholipid (DPPC) bilayer were used and we focused our attention on the effect of a singular S-NP and multiple S-NPs on the phase separation of the bilayers.

2 Methods

Simulation Details

Coarse-grained MD simulations were performed using GROMACS-5.0.1[32,33]. The short-range neighbour interaction list cut-off was fixed to 1.4 nm and updated every 10 steps. Non-bonded intermolecular interactions were described using a Lennard-Jones potential with the potential shifted to zero at 1.2 nm. Electrostatics were managed with a shifted potential and with a coulomb cutoff distance of 1.2 nm. The pressure was set to 1 atm and controlled using the semi-isotropic Parinello-Rahman scheme[34–36]. The temperature was set to 323 K and regulated using the Berendsen coupling scheme. Both schemes had a relaxation time of 1.25 ps. This temperature ensured the formation of phospholipid phase microdomain in the model bilayers[37–39]. Equilibration simulations were performed for 100 ns and production run simulations for 6 μs. An integration time-step of 0.01 ps was used throughout. Frames were recorded every 1×10^6 steps for analysis. Additional simulation parameters and equilibrium information are provided in the supplementary information.

MARTINI Force-Field Details

Atoms were encoded and unified into coarse-grained (CG) beads using the MARTINI forcefield[40]. This forcefield has extensive support for surfactant molecules, biomolecules, polymers, and nanoparticles. Each bead represents up to four atoms and are unified into one of four types: polar, nonpolar, apolar, or charged, corresponding to the labels P, N, C, and Q, respectively. Hydrogen atoms associated with heavy atoms are represented as part of the single interaction center. Bead types used for each lipid species are shown in Figure 1(a). The non-bonded interactions were parametrized using experimental partitioning free energies between polar and apolar phases of a large number of chemical compounds. The bonded interactions were derived from all-atom simulations.

Model Construction

The initial bilayer conformations were constructed using the *INSANE* lipodomics (*INSert membraNE*) tool[41]. This tool provides a convenient way to adjust the size and composition of a MARTINI model bilayer and position biomolecules and NPs within the bilayer. Model bilayers were constructed from cholesterol (CHOL) and three phospholipid species: dipalmitoylphosphatidylcholine (DPPC), saturated; decadienoylphosphatidylcholine (DUPC), double unsaturated; and dioctadecatrienoylphosphatidylcholine (DFPC), triple-unsaturated (Figure 1(a)). The three bilayer compositions presented in this study were DPPC-CHOL, DPPC-DFPC-CHOL and DPPC-DUPC-CHOL with two unit cell sizes. The first had dimensions of 15 nm^2 and then the seconnd was replicated in the x and y dimension to create a 30 nm^2 bilayer. The z dimension was 9 nm in both systems. Each bilayer system contained 30 % cholesterol with the exception of an additional DPPC model to act as a cholesterol-free control. Standard MARTINI water molecules were used to solvate each system and 15 % of the water molecules were replaced at random with counter ions to yield a net-zero charged system.

The S-NP topology was constructed using the micelle topology following the packing strategy of Packmol[42]. The innermost beads were treated as inert metal atoms and the closest metal beads were treated with harmonic bond potentials with a force

constant of 5000 kJ mol^{-1} to ensure their rigidity. A harmonic bond potential force constant of 1250 kJ mol^{-1} with an equilibrium bond length of 0.47 nm and a cosine angle potential of 180° with a force constant of 25 kJ mol^{-1} was applied to the bonds in the ligand. The S-NP[43] was constructed using charged and hydrophobic ligands (Figure 1(b)). A link to the S-NP parameter files can be found in the supplementary information.

The 15 nm^2 bilayer contained a single S-NP and the 30 nm^2 bilayer contained four S-NPs. The single S-NP was positioned within the centre of geometry of each bilayer and each of the four S-NPs were positioned equidistant from one another. The choice of ligands was similar to models by Simonelli *et al*[44], in which ligands based on octanethiol ligands (hydrophobic) and mercaptodecanesulfonate ligands (anionic) were used. Furthermore, in earlier studies the MARTINI force field had been used to design a general ligand-functionalized charged/hydrophobic S-NP using the hydrophobic C beads, and negatively charged Qa beads[45,46]. The length of each ligand type was approximately 1.7 nm, while the radius of the S-NP core was approximately 0.7 nm giving an approximate diameter of 4.1 nm (although this can fluctuate due to interactions with the water and phospholipid environment).

Each bilayer with S-NP model was subjected to a series of equilibration steps. Steepest descent minimisation was performed to resolve steric clashes. This was followed with a 100 ns simulation using the NVT ensemble (constant number of particles (N), volume (V) and temperature (T)) over an increasing timestep from 0.0001 ps to 0.01 ps using the velocity-verlet integration algorithm at 10 ns intervals[47–50]. The simulation was then extended for 6 μs using an NPT ensemble (constant number of particles (N), pressure (P) and temperature (T)). The first 1 μs of production simulation data were discarded from the analysis. The list of simulations presented in this study is summarised in Table 1.

2.1 Analysis

The GROMACS tools developed by Castillo *et al.*[51] were used to calculate the phospholipid tail order parameter (defined as $P_2 = \frac{1}{2}\langle 3\cos^2\Theta - 1\rangle$, where Θ is the angle between the bond vector and the membrane normal) and average density. The simulation unit cell was divided into 1 nm^2 cells over a two-dimensional grid covering the $x \times y$ plane. The phospholipid tail order parameter and the phospholipid density were averaged within each cell and reported. Cartesian components of the pressure tensors were calculated using the custom GROMACS[52,53] distribution. The simulation unit cell was divided into 1 nm^2 cells across the bilayer normal and lateral plane and the local pressure tensors P_{xx}, P_{yy}, P_{zz} were calculated across the the normal and lateral plane. The custom GROMACS software only returned average values without an indication of error. We therefore reported standard error of the mean by using binned averages. From the pressure tensor components we calculated the normal and lateral pressure across the profiles from the relations $P_L = -(\sigma_{xx}+\sigma_{yy})/2$ and $P_N = -\sigma_{zz}$. The line tension was calculated as $\gamma_p = \frac{1}{2}\left(P_{\text{per}} - P_{\text{par}}\right) L_z L_{\text{par}}$, where P_{per} and P_{per} are pressure tensor components perpendicular and parallel to the phase interface, respectively. The L_{per} and L_{par} are the box dimensions in the bilayer normal direction and the bilayer lateral direction, respectively.

The orderphobic effect of the NPs[54] was estimated using the Nelson-Halperin 2D bond-orientation order parameter[55,56], which acts as a useful metric for measuring the packing degree of lipids. The average hexagonal packing parameters of the top and bottom phospholipid leaflets were calculated using

$$\phi_l = \left| \left(\frac{1}{6}\right) \sum_{j \in nn(k)}^{n} \exp(6i\theta_{kj}) \right|^2, \quad (1)$$

where, θ_{kj} represents the angle between an arbitrary vector (in this case, we have used the y unit vector) and the hexagonal vertices, as illustrated in Figure 1(c). The six closest phospholipid carbon-chain beads were used to calculate the extent of 2D-disorder around the S-NP. An equilibrium average of one represents a perfect hexagonal packing and zero represents disordered packing. The phospholipid beads C2A/C2B and D2A/D2B (where A and B labels represent the two hydrophobic tails) in the phospholipid tail groups were used as points of reference with respect to the arbitrary vector[57]. All visualisations and analysis were implemented using a combination of VMD[58], APLVoro[59] and MDAnalysis[60], along with in-house scripts.

3 Results

Each model was left to equilibrate for 1 μs (equilibration data provided in Figure S1) followed by production runs for 5 μs. Each equilibrated trajectory was used to calculate, relative to the bilayer normal across the unit cell, the average mass density and phospholipid tail order parameters. Also, 2D lipid order parameters using the C2/D2 beads in the hydrophobic chain of DPPC, DUPC and DFPC phospholipids were calculated. Order parameters were used as a measurement of phospholipid order at the bilayer interface with the S-NP. Pressure tensor calculations were performed to show differences in the line tension between bilayer phases. Finally, the area-per-lipid (APL) and bilayer thickness were measured in the multi-S-NP simulations to identify phospholipid domain formations and bilayer deformations as the S-NPs approached a bilayer phase interface.

In the absence of S-NPs, both the DPPC-DUPC-CHOL simulations failed to reveal phospholipid phase separation, whereas phase separation was observed in the DPPC-DFPC-CHOL model bilayer (Figure SI 2).

3.1 Single S-NP

Single S-NPs in monomeric and two mixed-phospholipid bilayers, underwent production simulations for 5 μs (Figure 2). Average mass density and phospholipid tail order calculations were taken at time points where we observed a stable conformation (Figure 3 (a), (b) and (c)).

The phospholipid tail order parameter (Figure 3 (a)) of the DPPC and cholesterol combination is lower among the annular phospholipids (those local to the S-NP) and assumes a phospholipid tail order indicative of a bulk DPPC bilayer approximately 2 nm from the bilayer-S-NP interface. The average phospholipid density is greatest in the bulk bilayer.

The mixing of phospholipids DPPC with DUPC (Figure 2 (b))

Table 1 A catalogue of simulations preformed showing the initial bilayer size, number of S-NPs, the quantity of phospholipids and cholesterol, and the phospholipid ratio.

Simulation	Bilayer Size	NPs	DPPC	DUPC	DFPC	CHOL	Ratio
DPPC-CHOL-NP	15 nm^2	1	476	0	0	204	7:3
DPPC-DUPC-CHOL-NP	15 nm^2	1	272	204	0	204	4:3:3
DPPC-DFPC-CHOL-NP	15 nm^2	1	261	0	195	195	4:3:3
DPPC-CHOL	30 nm^2	0	1088	0	816	816	4:3:3
DPPC-DUPC-CHOL	30 nm^2	0	1088	0	816	816	4:3:3
DPPC-DFPC-CHOL	30 nm^2	0	1088	816	0	816	4:3:3
DPPC-4NP	30 nm^2	4	1906	0	0	0	NA
DPPC-CHOL-4NP	30 nm^2	4	1906	0	0	816	7:3
DPPC-DUPC-CHOL-4NP	30 nm^2	4	1088	816	0	816	4:3:3
DPPC-DFPC-CHOL-4NP	30 nm^2	4	1044	0	780	780	4:3:3

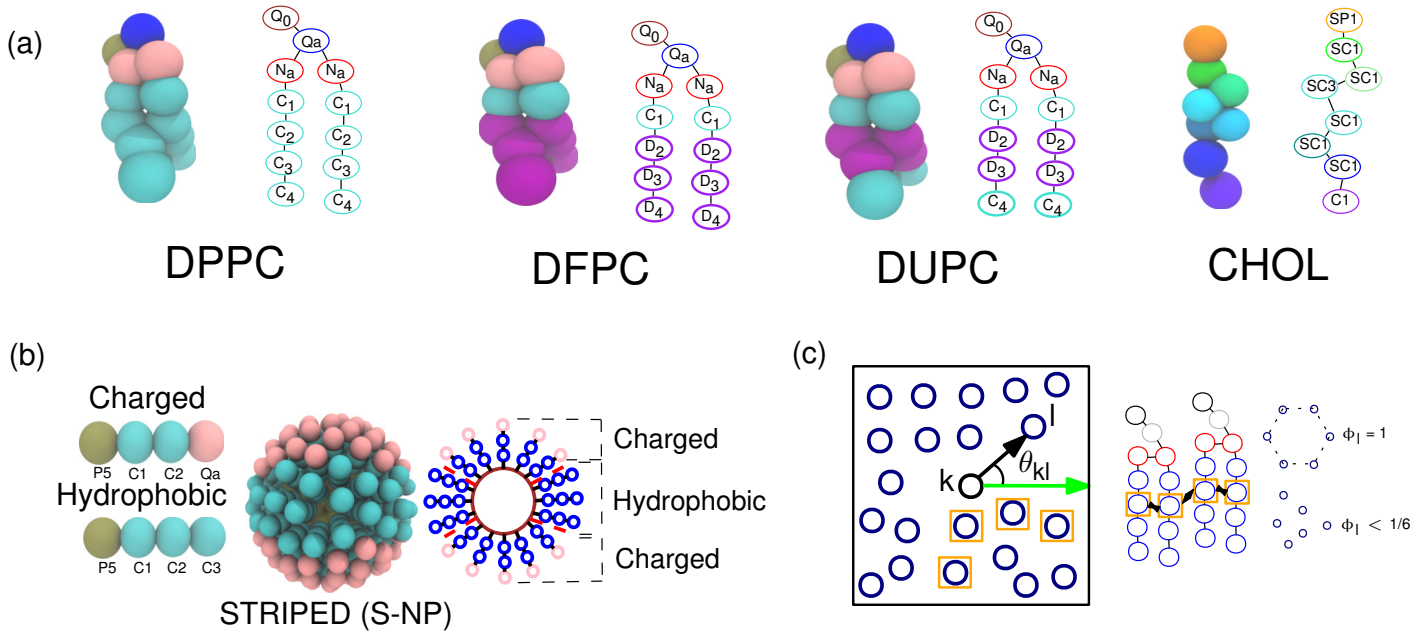

Fig. 1 (a) The MARTINI bead composition of each phospholipid type and cholesterol. Cyan beads represent grouped saturated carbons, purple for 1-2 cis double bonds, pink denotes the glycerol linker region, the blue bead the phosphate, and brown represents choline. (b) The schematic of the S-NP, which consists of a hydrophobic center stripe capped with charged ligands. (c) The orderphobic effect is calculated between an arbitrary reference vector and the C3/D3 beads of neighbouring phospholipids.

resulted in saturated and unsaturated microdomain formation within the first 100 ns with a consistent clustering of DUPC phospholipids around the S-NP. The phospholipid tail order parameter and mass density are similar to the values seen in the monophospholipid system, in that phospholipid order increases further from the S-NP, however, the difference between DUPC and DPPC introduces a greater degree of variance in phospholipid tail order. Within the time frame observed, the phospholipid microdomains consistently rearranged as phospholipids exchanged between domains. The mixing of phospholipids DPPC and DFPC (Figure 2 (c)), resulted in the formation of two phospholipid domains with cholesterol predominately found within the ordered, more dense, DPPC domain. The DFPC domain, containing the S-NP, had significantly less ordered phospholipid tails which corresponds well with the distribution of phospholipid mass density. The DPPC-DFPC interface presents a gradient in phospholipid tail order with lipids closest to the S-NP, more disordered than those further away.

The 2D bond order is a measurement of phospholipid packing order and was calculated from the phospholipid-S-NP interface into the bulk bilayer. The packing order (Figure 3 (d)) of the monophospholipid system, DPPC-CHOL, converges to a bulk arrangement within the first 0.5 nm from the phospholipid-NP interface. DPPC-DUPC-CHOL presents a sporadic arrangement of phospholipid packing, indicative of the formation of many small phospholipid-microdomains within DUPC lipids present local to the S-NP. The phospholipid order converges after 4 nm from the phospholipid-S-NP interface. The phospholipid arrangement within the DPPC-DFPC-CHOL bilayer comprises two regions with different phospholipid packing order, as a result of the formation of the two phospholipid microdomains.

The time-averaged phospholipid order parameter was measured from the centre-of-mass (COM) of the S-NP (Figure 3 (e)). The low order parameter values across the initial 2 nm are due

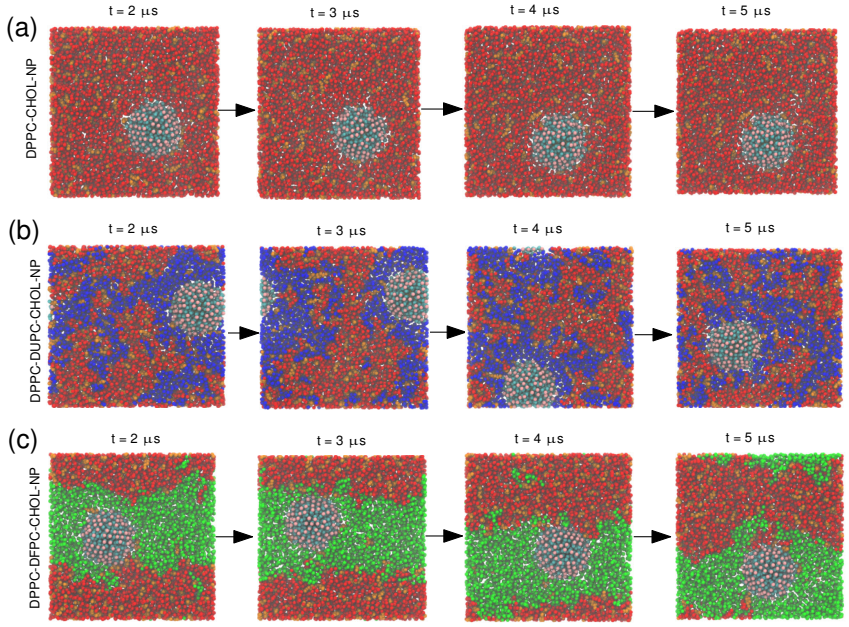

Fig. 2 Snapshots illustrating the evolution of each single S-NP bilayer system in the *xy* plane after equilibration. DPPC is red, DUPC blue, DFPC green and cholesterol is orange. Water has been removed for clarity.

to the measurement being made from the S-NP COM. The large degree of variance at 2 nm is due to fluctuations in the bilayer promoting a degree of exchange of phospholipids within this narrow space. The phospholipid order parameter of the unsaturated phospholipids, DUPC and DFPC, is consistently lower than the saturated DPPC across the unit cell. Whilst the order parameter of the unsaturated phospholipids remained constant, the order parameter for DPPC steadily increased the further from the S-NP indicating that the S-NP has a distorting effect on saturated lipid tails in close proximity to the S-NP, presumably as they distort to pack around the S-NP.

We calculated the x, y, and z components of the lateral and normal bilayer pressure profiles. An average was taken through the bilayer interface (x as defined by the distinct bilayer microdomain interface formation in DPPC-DFPC-CHOL) across each simulation and found pressure profiles dependent on the bilayer composition. In the lateral bilayer pressure (Figure 4 (a)), the P_{yy} and P_{zz} components in each bilayer fluctuated around 300–500 bar for the DPPC-DUPC-CHOL-NP and DPPC-DFPC-CHOL-NP systems, and 500 bar for the DPPC-CHOL-NP system. The P_{xx}, P_{yy}, and P_{zz} component (dimension parallel to the bilayer) presented a profile dependent on the S-NP and the phospholipid bilayer composition. In DPPC-CHOL bilayer, pressure peaks are local to the phospholipid-S-NP interface before decreasing by approximately 200–400 bar (5–7 nm), whilst in bulk, the pressure fluctuates between 0–1000 bar.

The pressure peaks on either side of the S-NP (10–12.5 nm) in DPPC-DUPC-CHOL show an increase of 300–600 bar. With the formation of two distinct bilayer microdomains in DPPC-DFPC-CHOL, the DPPC and cholesterol domain demonstrates a consistent $P_{xx}/P_{yy}/P_{zz}$ pressure profile from approximately 250 bar to 500 bar. We see a large peak in P_{zz} of approximately 1500 bar from 0 nm to 2.5 nm. This is located near the domain interface of the DPPC-CHOL and DFPC with the S-NP in contact. Where the S-NP is not interacting with the domain interface (10–11 nm), we see a small dip in the pressure by approximately 250 bar. The pressure profiles calculated normal to the bilayer (Figure 4 (b)), fluctuate consistently around 0 bar in the P_{yy} and P_{zz} component. Averaged along the x axis, there are two distinct peaks of negative pressure approximately level with the hydrophilic phospholipid head groups. The pressure increases in the bilayer core. The lower pressure peaks in the monophospholipid DPPC and cholesterol bilayer construct are due to the homogeneous phospholipid composition. The lateral (P_{yy} and P_{xx}) and normal pressure profiles averaged along the bilayer normal (Figure 4 (c)), remain consistent with the trend of their individual pressure tensors.

The line tension between phases was estimated using the $\frac{1}{2}(P_{per} + P_{par})$ pressure profile calculations. We computed an upper estimate change in pressure of approximately 50 bar near the domain interface for the DPPC-DUPC-CHOL-NP system (an approximate upper estimate of 3.375×10^{-10} N for the line tension) and an upper estimate of approximately 75 bar for the DPPC-DFPC-CHOL-NP system (an approximate upper estimate of 1.125×10^{-9} N for the line tension). The line tension can be used to calculate the free energy of adsorption of the domain boundaries by the NPs using:

$$\Delta G_{\text{adsorption}} = 2\lambda R, \tag{2}$$

where λ indicates the line tension, and R is the radius of the NP[61]. When using a radius of between 2 and 2.5 nm the adsorption energy of the NPs to the interface is between 6.750×10^{-19} and 8.437×10^{-19} J for the DPPC-DUPC-CHOL-NP, and between 2.025×10^{-18} and 2.531×10^{-18} J for the DPPC-DFPC-CHOL-NP system.

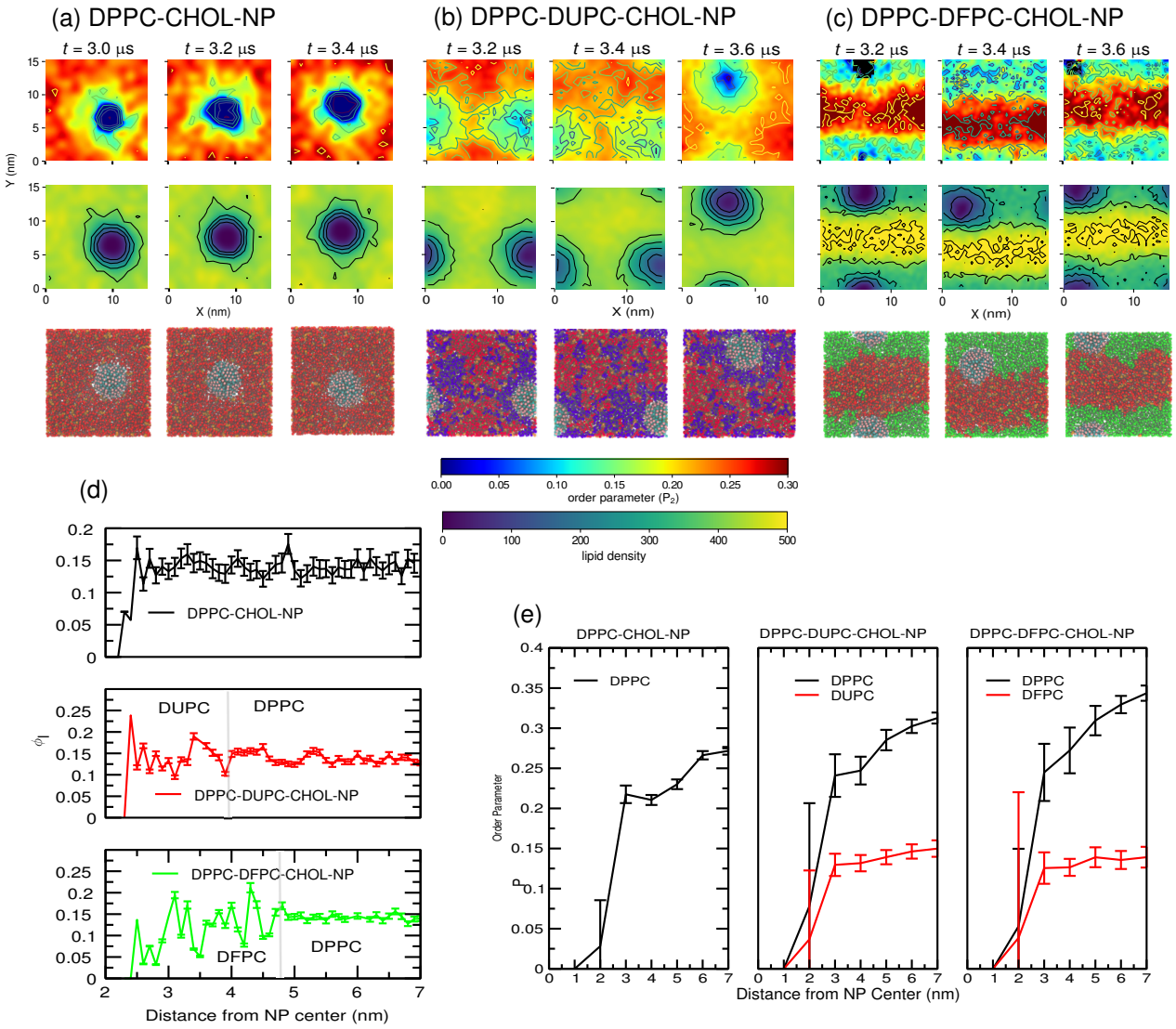

Fig. 3 Three frames showing the phospholipid tail order parameter (top) analysis and average mass density (middle) of the three single S-NP systems, (a) DPPC-CHOL, (b) DPPC-DUPC-CHOL and (c) DPPC-DFPC-CHOL. Each frame was selected as a representative of the system at equilibrium. (d) The 2D order parameter of the bilayer as a function of distance from the S-NP COM. The position of the interface is indicated with a grey line. (e) The phospholipid tail order parameter of individual phospholipid types as a function of distance from the S-NP COM. Each data point was calculated as an average over 1000 ns. Error bars represent the standard error of the mean.

3.2 Multiple S-NPs

Production runs of 5 μs were performed for each model bilayer construct with multiple S-NPs. The average mass density and phospholipid tail order parameter calculations were taken when each system was seen to adopt a stable conformation (snapshots of the simulations are shown in Figure 5). Short animations of each simulation has been provided as part of the supplementary information.

To determine whether the presence of cholesterol would affect nanoparticle aggregation we also performed an NPT simulation of four S-NPs in a pure DPPC bilayer without cholesterol for 5 μs. The initial placement of the S-NPs were identical to those in the DPPC system with cholesterol. The NPs were shown to aggregate shortly after 4 μs.

In the DPPC-CHOL-4NP simulation (Figure 6 (a)) a decreasing order parameter was observed local to the S-NPs, approximately 0.17 nm from the phospholipid-S-NP interface. The analysis was performed over three stable configurations after the S-NPs were shown to aggregate within the initial 100 ns. The average mass density was consistent throughout the bulk bilayer at 400–500 kg m^3 but dropped to 250–300 kg m^3 within the phospholipids local to the S-NPs. This difference demonstrates ordered packing in the bulk bilayer and disorder local to the S-NPs.

The DPPC-DUPC-CHOL-4NP simulation showed a reduction in the phospholipid tail order parameter through a gathering of unsaturated DUPC phospholipids around the S-NP whilst cholesterol migrated into the saturated DPPC regions. The average mass density remained consistent throughout the simulation, with a sharp decrease in density similar to the decrease in phospholipid tail order local to the S-NP aggregate.

During the simulation of the DPPC-DFPC-CHOL-4NP system, a DFPC phospholipid microdomain formed within the initial 100 ns

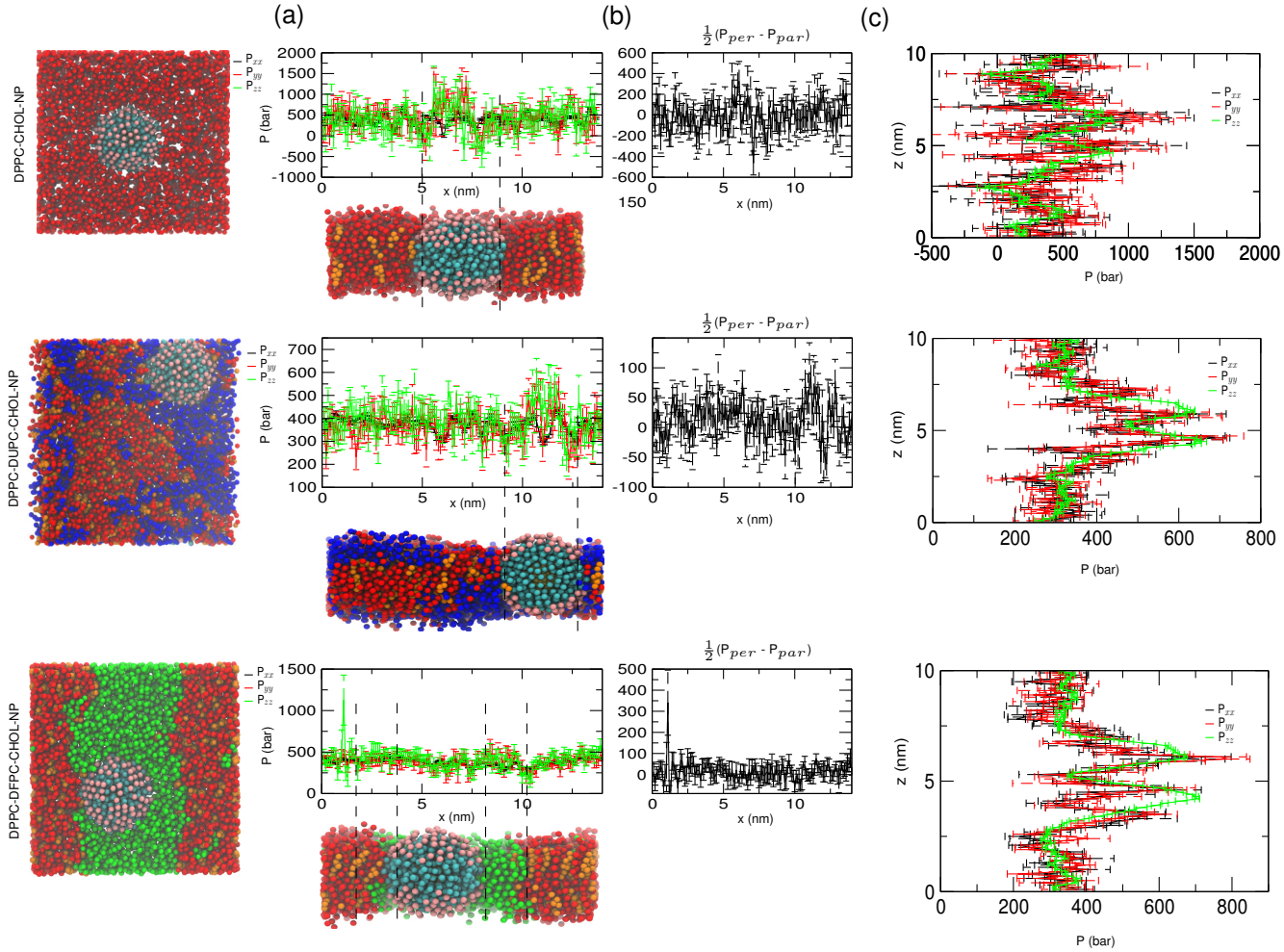

Fig. 4 The individual components to the pressure tensor (P_{xx}, P_{yy}, P_{zz}) along the bilayer normal and lateral plane for DPPC-CHOL, DPPC-DUPC-CHOL, and DPPC-DFPC-CHOL (a), along with the $\frac{1}{2}(P_{per} + P_{par})$ from the bilayer lateral plane (b), and the pressure tensor components from the bilayer normal (c). Measurements were calculated using block averages from 4.5 μs to 5 μs and error bars represent standard error of the mean.

around the NPs, stabilising the S-NP aggregate whilst the complete phase separation as presented in Figure 6 (c) occurred. We see a gradient of order parameters between the unsaturated DFPC and the saturated DPPC domains. There is a clear mass density difference between the two phospholipid domains, with DPPC-CHOL showing the greater mass density compared to the DFPC microdomain. The difference in mass density at the phospholipid-NP interface is very slight, similar to the difference in phospholipid order, suggesting the favourable inclusion of the S-NPs in the DFPC microdomain.

The averaged APL and phospholipid length as a function of time are shown in Figure 6 (d).For the DPPC-CHOL-4NP simulation the area of cholesterol had a value of 0.42 nm^2 and the DPPC had a higher area of 0.52 nm^2. The cholesterol thickness was 3.4 nm, while the DPPC thickness was 4.2 nm. Each APL of the DPPC-DUPC-CHOL-4NP model remained consistent. Cholesterol had the smallest area (0.45 nm^2), followed then by the saturated DPPC phospholipid (0.53 nm^2) and finally, the DUPC phospholipid (0.65 nm^2), which follows the kinked nature of the DUPC phospholipid allowing for a larger area. The bilayer thickness as an average measurement between identical phospholipid types is quite clear; the saturated DPPC yields the greatest thickness (4.2 nm), followed by the unsaturated DUPC phospholipid (3.95 nm) and finally cholesterol (3.4 nm).

The APL of cholesterol and DPPC in the DPPC-DFPC-CHOL-4NP simulation are very similar (0.42 nm^2 and 0.48 nm^2, respectively), whilst DFPC presents greater APL (0.65 nm^2). In terms of bilayer thickness, cholesterol and the DFPC phospholipids show similar ranges in lipid thickness (3.6–3.8 nm) and a larger thickness for the DPPC (4.3 nm). We also observe the effect of the S-NPs on the local cholesterol density (Figure 6 (e)); we see a minimal change in the cholesterol density for the DPPC-CHOL-4NP system (with a peak RDF value of approximately 1.1), whilst we see distinctive and decreasing densities of the cholesterol around the NPs in the DPPC-DUPC-CHOL-4NP and DPPC-DFPC-CHOL-4NP (where the values of the radial distribution function (RDF) decreases from approximately 0.8 to 0.4 (DPPC-DUPC-CHOL-4NP) and from 0.5 to 0.2 (DPPC-DFPC-CHOL-4NP)). A similar trend was observed around the S-NPs between the cholesterol mass fraction and the RDF profiles (Figure 6 (f)). In the DPPC-CHOL-4NP system the mass fraction of cholesterol remained consistent at approximately 10% over the course

of the simulation. The mass fraction increased further from the S-NPs. In both DPPC-DUPC-CHOL-4NP and DPPC-DFPC-CHOL-4NP simulations, we observed an increase in cholesterol mass fraction beyond 10 nm from the S-NP centers.

We analysed the bilayer thickness of each mixed bilayer simulation by calculating the average phospholipid length as a function of distance from the centre of each S-NP (Figure 7). To account for the arrangement of the bilayer components, the phospholipid length calculations were block averaged per 1 μs and variation in length was obtained using the standard error of the mean. The spread in phospholipid length was consistent after accounting for those phospholipids at the S-NP interface. The spread in DPPC length is consistent across all three systems, yet DPPC phospholipids were longer when they were not mixed with other phospholipids (Figure 7 (a)). After the initial 1μs, the average DFPC length unevenly distributes from the S-NP with the average length peaking approximately 15 nm from the S-NP (Figure 7 (b)). Once the DPPC-DUPC mixed bilayer forms the two distinct phospholipids domains, the DUPC component remains consistent shorter (Figure 7 c)). There is little difference in length then between bulk DUPC and those at the S-NP interface.

4 Discussion

We performed several simulations of hydrophilic-hydrophobic ligand functionalized striped nano-particles in mixed bilayers of DPPC, DUPC, DFPC and cholesterol along with the monophospholipid DPPC bilayer with cholesterol and finally, with only DPPC. The mixed bilayers were chosen to simulate near and certain phase separating systems. Our simulations show nanoparticle aggregation near unsaturated phospholipid regions, phase separation promoted in the presence of nanoparticles, and the role mixed-bilayers play in the lateral organization of nanoparticles.

In a previous Monte Carlo simulation study, nanoparticles fused with a mix of charged and hydrophobic ligands enter the bilayer interior through the interactions between the charged ligands and the hydrophilic headgroups of the bilayer[25]. The placement of the NPs within the bilayer is stabilized by a 'snorkelling' effect. Observed 'snorkelling' of the local phospholipids induces a hydrophobic mismatch between the snorkelled phospholipids and the rigid cholesterol molecules, resulting in the depletion of local cholesterol density local to the NP[45,46]. From our single S-NP DPPC-DUPC-CHOL and DPPC-DFPC-CHOL simulations, we also observed local depletion of cholesterol corresponding with phospholipids exchange between DPPC and either DUPC or DFPC, which in turn drives the formation of a bulk DPPC-CHOL region away from the S-NP. Risseleda *et al.* revealed that cholesterol in phase-separated bilayers is enthalpically driven to maximize levels of intermolecular contact with saturated phospholipids tails[37], which corresponds to an additional driver for the aggregation of unsaturated phospholipids near the S-NP. In the case of the DPPC-DUPC-CHOL and single S-NP, the cholesterol depletion drives the DUPC aggregation near the S-NPs. The equilibrium simulation snapshots reveal the formation of an unsaturated semi-circular domain near the S-NP clusters (in the cases of DPPC-DUPC-CHOL and DPPC-DFPC-CHOL). As suggested by studies of mismatch energetics by Hu *et al.*[62], domain formation before full phospholipid phase separation occurs when the hydrophobic mismatch is significant. The domain formation with the DPPC-DUPC-CHOL bilayer only occurs with the inclusion of the S-NP, while it is fully observable in both the NP/NP-absent case with the DPPC-DFPC-CHOL bilayer, indicating a greater hydrophobic mismatch between the DPPC-DFPC bilayer compared to the DPPC-DUPC bilayer.

Adding an unsaturated DUPC or DFPC phospholipid component to a DPPC bilayer results in the NPs partitioning into the liquid-disordered region. This follows similar results as seen by previous studies of transmembrane helices[63]. This has been attributed to the favourable enthalpic interactions between tightly packed liquid-ordered phospholipids, which in turn drives the lateral sorting of protein helices. The packing in the liquid-ordered phase (DPPC-DPPC and DPPC-CHOL) is enthalpically favourable, and whilst the inclusion of the NPs into the liquid-disordered phase would be expected to increase the global entropy of the mixed bilayer, the enthalpic penalty of disrupting the liquid-ordered region prevents any aggregation of the NPs in the liquid-ordered region.

The absence of unsaturated lipids in the multiple S-NPs DPPC-CHOL simulation demonstrated a delay in the formation of the S-NP clover-like aggregation compared to both DPPC-DUPC-CHOL and DPPC-DFPC-CHOL simulations. The aggregation of S-NPs can be seen to be analogous to those of membrane proteins; Parton *et al.*[64] demonstrated the effect of hydrophobic mismatch on α-helical transmembrane (TM) proteins, and indicated that phospholipid demixing occurs around the proximity of the TM proteins occur resulting in the aggregation of phospholipids around the proteins where the contact between the hydrophobic chains and the hydrophobic tailgroups of the phospholipids was maximised. In the case of the DPPC-CHOL simulation the bilayer demixing displaces the cholesterol molecules from around the NP.

Another interesting point of note is the difference between the clover-like arrangement of the S-NPs we observed and of those of a linear arrangement in the simulations by Angelikopoulos *et al.*[45,46]. The increase in hydrophobic ligand length in their models maximised hydrophobic surface area, which hindered the snorkelling of hydrophilic ligands and increased hydrophobic contacts with the annular phospholipids. This would suggest the orderphobic effect may be a driver for the clover-like cluster.[54]. This phenomena closely follows the aggregation mechanism of transmembrane proteins and protein-mimics due to the orderphobic effect, which can determine the aggregation of protein-like structures due to the formation of a local order-disorder interface.

Our cholesterol-free DPPC simulation revealed a single stable interaction between two of four S-NPs after 2 μs. The association between nanoparticles in the absence of cholesterol is not unexpected as the order-disorder region around the NPs is still present in the absence of cholesterol. Compared to the study by Angelikopoulos *et al.*[45,46], where NP aggregation is not observed, the differing length of the hydrophobic ligands on the NP surface may increase the order-disorder interface around the NPs. This is indicated in Figures S1 and S2.

Similar orderphobic effects have been observed in Influenza A matrix 2 transmembrane protein which induce local membrane

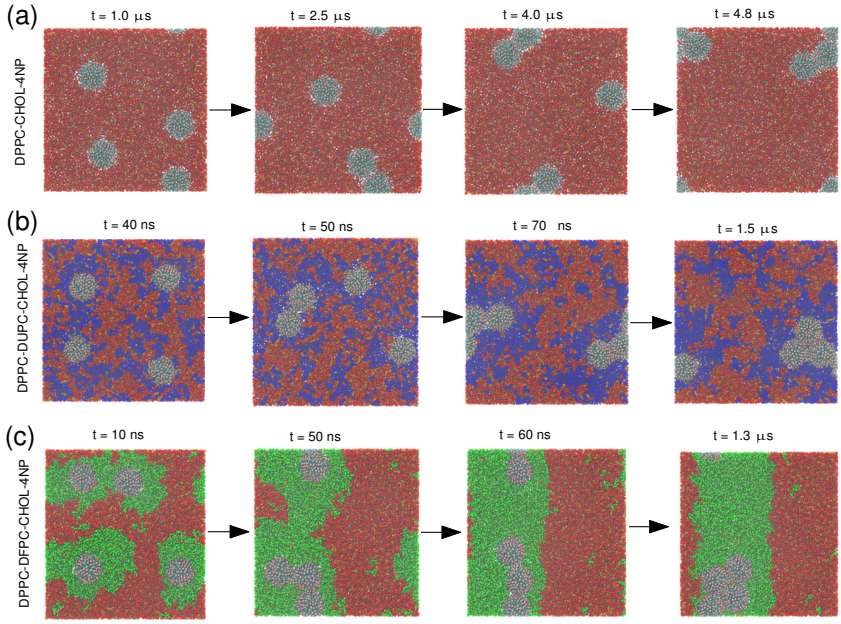

Fig. 5 Single time frames illustrating the change to the bilayer and aggregation of the NPs as each system evolves. DPPC is red, DUPC blue, DFPC green and cholesterol is orange. Water has been removed for clarity

remodelling by the aggregation of proteins[65,66]. The M2 protein lowers the hydrophobic tail order parameter at tail end termini for both 'stiff' and 'soft' phospholipids. This corresponds with the lowered phospholipid tail order parameters for the DPPC, DUPC and DFPC phospholipids in our simulations.However, the significant difference in electrostatic surface charge between these membrane proteins and the striped-nanoparticles in this study must be considered. Given the charged S-NP ligands, one might expect electrostatic repulsion between S-NPs rather than the aggregation observed in this study. It is entirely plausible that the energetic gain from the reduction in the line tension overcomes the energetic penalty incurred from electrostatic repulsion between nanoparticles.

Ollila *et al* studied the pressure profile surrounding the mechanosensitive protein channel of *Mycobacterium tuberculosis*. The monolayers surrounding the protein[67,68] show a lower lateral tension and the formation of spontaneous curvature due to this would cause the redistribution of lipids around the protein. We see a variety of similar effect on the pressure tensor components near the lateral pressure of the NP. In the monophospholipid DPPC-CHOL bilayer, there is a drop in pressure within the S-NP region, while in the mixed DPPC-DUPC-CHOL and DPPC-DFPC-CHOL bilayers we observe a distinct feature in the pressure profile at the lateral position of the S-NP. This suggests that an S-NP at the phospholipid domain interface; firstly, lowers lateral pressure and secondly, the increase of lateral pressure due to a reorganization of phospholipids in monolayer regions further from the phospholipid domain region. In the DPPC-DUPC-CHOL bilayer, we see the formation of small DUPC phospholipid microdomains in the vicinity of the S-NP. This corresponds to the highly fluctuating orderphobic region seen 2.0–4.0 nm of the S-NP center. This analogous region is absent in the DPPC-DFPC-CHOL case, but we suggest that this is due to the linear domain boundary formed near the S-NP region, which would result in the collective average of the stable and fluctuating phases in the DPPC-CHOL and DFPC regions formed.

Following this, in the case of the DPPC-DUPC-CHOL simulation, the reduction in size of the line tension interface drives the aggregation of S-NP into a clover formation, while in the DPPC-DFPC-CHOL bilayer, we see how rapid domain formation drives the aggregation of S-NPs. Similar aggregation behaviour has been seen in transmembrane proteins. For example, Yoo *et al.*[69] demonstrated that for the association of gA proteins, two factors were noticeable, the compression of the phospholipids in between the proteins leading to a higher energy barrier of association and the depletion of local phospholipids increasing the fluidity of the proteins. It was also observed that typically, clusters of at most four proteins were seen. When comparing to our study, we suggest that the local disordering of phospholipids around the S-NPs, induced by the hydrophobic mismatch between the DPPC and DUPC-DFPC and the favourable interaction between the DPPC and cholesterol, drives the aggregation of unsaturated phospholipids within the vicinity of the S-NP. The subsequent aggregation between S-NPs is driven by the reduction of the energetically unfavourable domain interface between the liquid-disordered and the liquid-ordered domains in the DPPC-CHOL region. Experimental measurements of the line tension range in the region 0.2–6.2 $\times$ 10^{-12} J m^{-1} (0.2–6.2 $\times$ 10^{-12} N)[70–72]. Lipowsky[73] computed a crude estimate of 10^{-17} J μm^{-1} = 10^{-11} N, and simulation studies by Rosetti *et al.*[74] measured values in the range 28–32 pN (2.8–3.2 $\times$ 10^{-11} N) in the domain boundaries between DAPC and DPPC. These values are notably lower than the estimates extracted from the values we have observed. However, it is worth noting that the lateral and normal pressure fluctuation is very large, hence our values only give the upper estimate of the line tension, and would be expected to fluc-

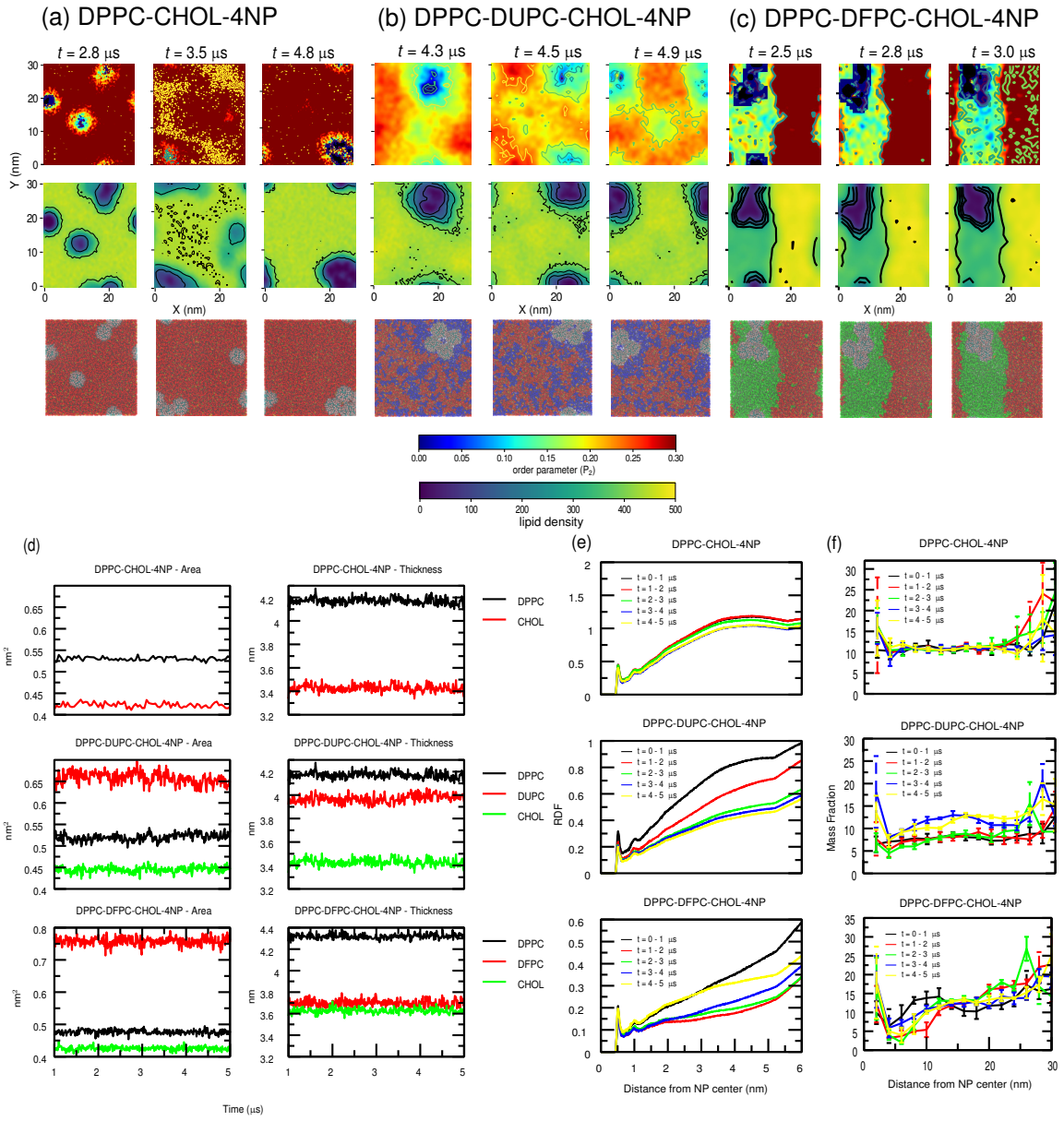

Fig. 6 Simulation snap-shots showing four S-NPs in each of the model bilayers (a) DPPC-CHOL, (b) DPPC-DUPC-CHOL and (c) DPPC-DFPC-CHOL along with corresponding phospholipid order parameters and mass density plots. Calculation of the APL by phospholipid type (d) and the RDF profiles of cholesterol from the S-NPs by 2 Å intervals (e), and the mass fraction of cholesterol (f).

tuate near the computed values from previous studies.

Finally, we expect NP aggregation to occur due to a contributing combination of ionic ligands minimizing interaction with ionic beads whilst maximising the hydrophobic interaction between the ligands and the lipid interior. The energetic gain from the reduction of line tension surface area is greater than the energetic penalty from the Coulombic repulsion between the S-NP ligands. It would be possible in future work to test further effects on aggregation in a bilayer by reducing the surface area of the NP core and replace hydrophobic ligands with ionic ligands.

5 Conclusions

From this study, we have observed how an orderphobic effect between the S-NPs and the immediate lipid environment is a driving force for S-NPs to aggregate with disordered regions in mixed bilayers. We have demonstrated that the hydrophobic mismatch between local phospholipids and the S-NPs drive annular phospholipid aggregations, which presents evidence of local cholesterol depletion, resulting in the aggregation of unsaturated domains near the S-NPs.

The author's are unaware of any direct comparable experimental studies of striped nano-particles. However, there are similarities between the results of the simulations presented and with a small number of experimental efforts. For example, Rasch *et al.* [75] undertook experiments of phosphatidylcholine vesicle formation with with dodecanthiol-coated Au NPs. These formed clusters within the vesicle bilayer space through a process described as 'zipping'. This observed zipping of NPs is quite similar to the local

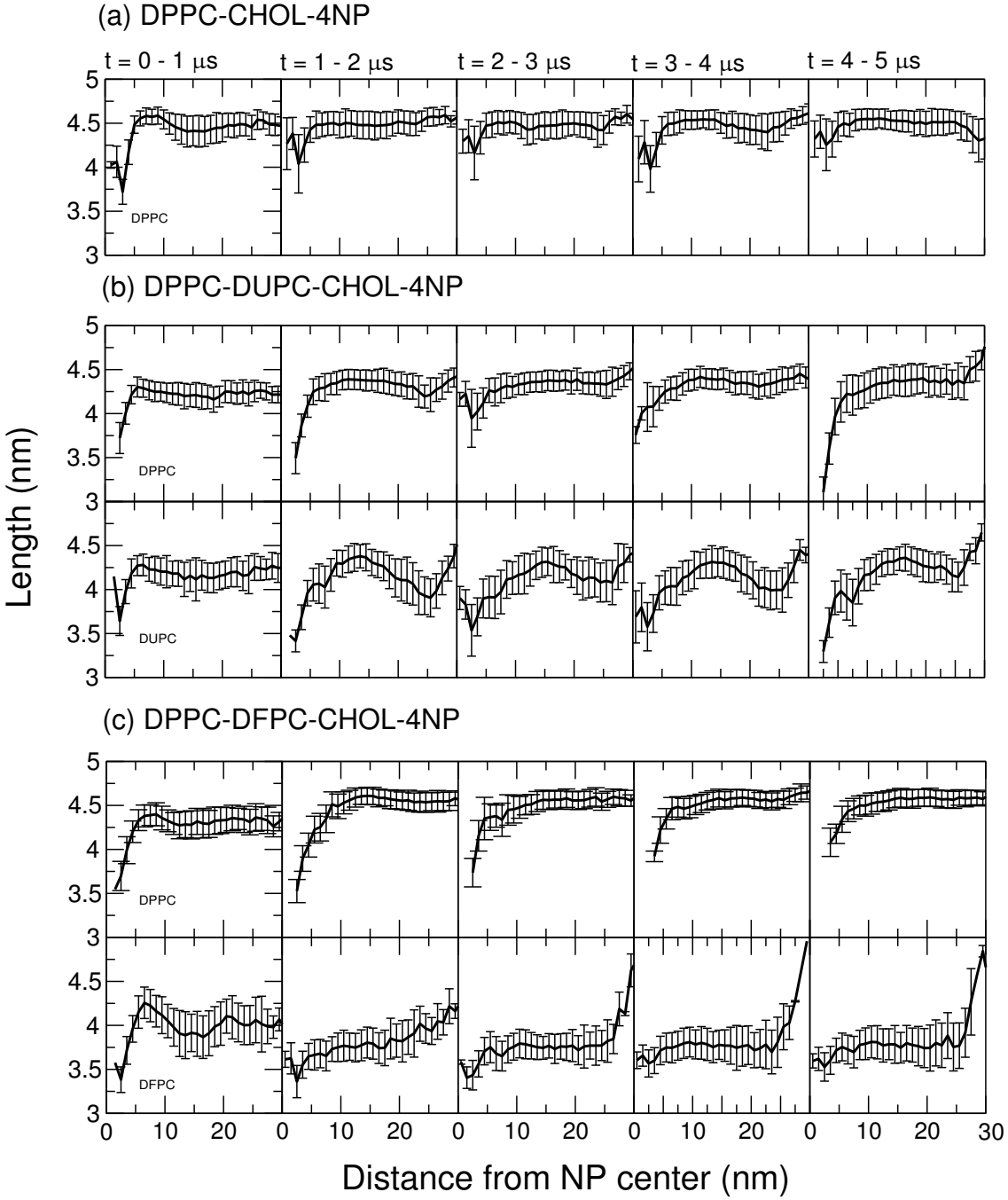

Fig. 7 The average bilayer thickness of each lipid component as a function of the distance from the center of each NP. Calculations were performed over the three 4-NP simulations, (a) DPPC-CHOL-4NP, (b) DPPC-DUPC-CHOL-4NP, and (c) DPPC-DFPC-CHOL-4NP. The average lipid thickness was calculated using 1 nm bins from the centre of mass of the NP and then averaged across the respective time spans. Error bars are presented using the standard error of the mean.

orderphobic effect around the NPs in our simulations, which also drives its aggregation with NPs, and also drives the local lipid-exchange around the NPs in mixed bilayers. Also, Guo *et al.*[76] showed that on a millisecond timescale, a lipid-coated hydrophobic AuNP can translocate into a lipid bilayer. It was also observed that NPs smaller than 5 nm stay embedded within the bilayer, whilst ones larger creates pores on the surface of the bilayer. This was experimentally observed using a DMPC and fluorescent DPPE lipid membrane on a microfluidic chip. This would indicate that it may not be necessary to have hydrophilic ligands attached on the surface of the NP for translocation to occur, and that aggregation can be driven by the reduction of the orderphobic/zipping radius around the NPs.

It is clear that the order-disorder interface around the S-NP structures does exist[54,77], however, we acknowledge that lipid order parameter calculations do not conclusively show an orderphobic effect in a phospholipid bilayer in the presence of S-NP. In summary, our study shows that the ligand-functionalized S-NPs

have an affect on the phospholipid conformation in mixed bilayer and an orderphobic effect contributes to the aggregation of S-NPs due to a reduction of the surface area contact with the ordered lipids. Our findings suggest lipid aggregates driven by of NPs may affect drug-delivery and may have an effect on the functionality of bio-molecules within the local lipid environment.

Conflicts of interest

There are no conflicts to declare.

Acknowledgements

We would like the acknowledge the Center for Scientific Computing (CSC) at the University of Warwick for computing resources required for this work.

Notes and references

1 T. M. Allen and P. R. Cullis, *Science*, 2004, **303**, 1818.
2 E. Blanco, H. Shen and M. Ferrari, *Nat. Biotechnol.*, 2015, **33**, 941–951.
3 H. Jang, *Molecules*, 2017, **22**, E2197.
4 M. Kang and S. M. Loverde, *J. Phys. Chem. B*, 2014, **118**, 11965–11972.
5 A. Dadwal, A. Baldi and R. K. Narang, *Artif. Cells Nanomed. Biotechnol.*, 2018, **46**, 1 – 11.
6 M. Werner, T. Auth, P. A. Beales, J. B. Fleury, F. Höök, H. Kress, R. C. Van Lehn, M. Müller, E. P. Petrov, L. Sarkisov, J. U. Sommer and V. A. Baulin, *Biointerphases*, 2018, **13**, 028501.
7 A. Walrant, S. Cardon, F. Burlina and S. Sagan, *Acc. Chem. Res*, 2017, **50**, 2968–2975.
8 B. J. Bennion, N. A. Be, M. W. McNerney, V. Lao, E. M. Carlson, C. A. Valdez, M. A. Malfatti, H. A. Enright, T. H. Nguyen, F. C. Lightstone and T. S. Carpenter, *J. Phys. Chem. B*, 2017, **121**, 5228–5237.
9 S. G. Aller, J. Yu, A. Ward, Y. Weng, S. Chittaboina, R. Zhuo, P. M. Harell, Y. T. Trinh, Q. Zhang, I. L. Urbatsch and G. Chang, *Science*, 2009, **323**, 1718 – 1722.
10 G. Rossi and L. Monticelli, *Adv. Phys-X*, 2016, **1**, 276 – 296.
11 K. Cho, X. Wang, S. Nie, Z. G. Chen and D. M. Shin, *Clin. Cancer Rese.*, 2008, **14**, 1310 – 1316.
12 R. R. Meka, S. Mukherjee, C. R. Patra and A. Chaudhuri, *Nanoscale*, 2019, **11**, 7931–7943.
13 S. Baoukina, E. Mendez-Villuendas and D. P. Tieleman, *J Am. Chem. Soc.*, 2012, **134**, 17543 – 17553.
14 E. London, *Biophys J*, 2016, **111**, 465 – 466.
15 F. Schmid, *Biochim. Biophys. Acta.*, 2017, **1859**, 509 – 528.
16 J. M. Crane and L. K. Tamm, *Biophys. J.*, 2004, **86**, 2965 – 2979.
17 S. O. Yesylevskyy, A. P. Demchenko, S. Kraszewski and C. Ramseyer, *Sci. World J.*, 2013, 1 – 10.
18 Q. Ong, Z. Luo and F. Stellachi, *Acc. Chem. Res.*, 2017, **50**, 1911 – 1919.
19 J. D. Gibson, B. P. Khanal and E. R. Zubarev, *J. Am. Chem. Soc.*, 2007, **129**, 11653 – 11661.
20 P. Pengo, M. Şologan, L. Pasquato, F. Guida, S. Pacor, A. Tossi, F. Stellacci, D. Marson, S. Boccardo, S. Pricl and P. Posocco, *Eur. Biophys. J.*, 2017, **46**, 749 – 771.
21 E. Colangelo, J. Comenge, D. Paramelle, M. Volk, Q. Chen and R. Lévy, *Bioconjugate Chem.*, 2017, **28**, 11 – 22.
22 S. Angeioletti-Uberti, *Npj Comput. Mater.*, 2017, **3**, 19 – 25.
23 S. Zhang, H. Gao and G. Bao, *ACS Nano*, 2015, **9**, 8655 – 8671.
24 H. Yuan, J. Li, G. Bao and S. Zhang, *Physical Review Letters*, 2010, **105**, 138101.
25 R. C. Van Lehn and A. Alexander-Katz, *J. Phys. Chem.*, 2014, **118**, 5848 – 5856.
26 R. C. Van Lehn, M. Ricci, P. H. Silva, P. Andreozzi, J. Reguera, K. Voïtchovsky, F. Stellachi and A. Alexander-Katz, *Nat. Commun.*, 2014, **5**, 4482.
27 R. C. Van Lehn and A. Alexander-Katz, *Soft Matter*, 2014, **10**, 648 – 658.
28 A. M. Jackson, J. W. Myerson and F. Stellacci, *Nat. Mater.*, 2004, **3**, 330 – 336.
29 X. Quan, C. Peng, D. Zhao, L. Li, J. Fan and J. Zhou, *Langmuir*, 2017, **33**, 361 – 371.
30 J. Barnoud, G. Rossi, S. J. Marrink and L. Monticelli, *PLoS Comput. Biol.*, 2014, **10**, e1003873.
31 C. M. Jewell, J. M. Jung, P. U. Atukorale, R. P. Carney, F. Stellacci and D. J. Irvine, *Angew. Chem. Int. Ed. Engl.*, 2011, **50**, 12312–12315.
32 H. J. C. Berendsen, D. van der Spoel and R. van Drunen, *Comp. Phys. Commun.*, 1995, **91**, 43 – 56.
33 M. J. Abraham, T. Murtola, R. Schulz, S. Páll, J. C. Smith, B. Hess and E. Lindahl, *SoftwareX*, 2015, **1-2**, 19 – 25.
34 M. Parrinello and A. Rahman, *Phys. Rev. Lett.*, 1980, **45**, 1196 – 1199.
35 M. Parrinello and A. Rahman, *J. Appl. Phys.*, 1981, **52**, 7182 – 1199.
36 M. Parrinello and A. Rahman, *J. Chem. Phys.*, 1982, **76**, 2662.
37 H. J. Risselada and S. J. Marrink, *Proc. Natl. Acad. Sci. U.S.A.*, 2008, **105**, 17367 – 17372.
38 R. S. Davis, P. B. Sunil Kumar, M. M. Sperotto and M. Laradji, *J Phys. Chem. B*, 2013, **117**, 4072 – 4080.
39 X. Chen, D. P. Tieleman and Q. Liang, *Nanoscale*, 2018, **10**, 2481 – 2491.
40 S. J. Marrink, H. J. Risselada, S. Yefimov, D. P. Tieleman and A. H. de Vries, *J. Phys. Chem. B.*, 2007, **111**, 7812 – 7824.
41 T. A. Wassenar, H. I. Ingólfsson, R. A. Böckmann, D. P. Tieleman and S. J. Marrink, *J Chem. Theory Comput.*, 2015, **11**, 2144 – 2155.
42 J. M. Martínez and L. Martínez, *J of Comput Chem*, 2003, **24**, 819–825.
43 X. Ge, P. C. Ke, T. P. Davis and F. Ding, *Small*, 2015, **11**, 4894 – 4899.
44 F. Simonelli, D. Bochicchio, R. Ferrando and G. Rossi, *J. Phys. Chem. Lett.*, 2015, **6**, 3175 – 3179.
45 P. Gkeka, P. Angelikopoulos, L. Sarkisov and Z. Cournia, *PloS Comput. Biol.*, 2014, **12**, e1003917.

46 P. Angeliopoulos, L. Sarkisov, Z. Cournia and P. Gkeka, *Nanoscale*, 2017, **9**, 1040 – 1048.

47 D. Frenkel and B. Smit, *Understanding Molecular Simulation: From Algorithms to Applications*, 2001.

48 D. C. Rapaport, *The Art of Molecular Simulation*, 2004.

49 L. Verlet, *Phys. Rev.*, 1962, **159**, 98 – 103.

50 C. W. Swope, H. C. Andersen, P. H. Berens and K. R. Wilson, *J. Chem. Phys.*, 1982, **76**, 637.

51 N. Castillo, L. Monticelli, J. Barnoud and D. P. Tieleman, *Chem. Phys. Lipids*, 2013, **169**, 95 – 105.

52 J. M. Vanegas, A. Torres-Sànchez and M. Arroyo, *J. Chem. Theory Comput.*, 2014, **10**, 691 – 702.

53 A. Torres-Sànchez, J. M. Vanegas and M. Arroyo, *Phys. Rev. Lett.*, 2015, **114**, 258102.

54 S. Katira, K. K. Mandadapu, S. Vaikuntanathan, B. Smit and D. Chandler, *Elife*, 2016, **11**, 13150.

55 B. I. Halperin and D. R. Nelson, *Phys. Rev. Lett.*, 1978, **41**, 121 – 124.

56 D. R. Nelson and B. I. Halperin, *Phys. Rev. B*, 1979, **19**, 2457 – 2484.

57 G. A. Pantelopoulos, T. Nagai, A. Bandara, A. Panahi and J. E. Straub, *J. Chem. Phys.*, 2017, **147**, 095101.

58 W. Humphrey, A. Dalke and K. Schulten, *J. Mol. Graph.*, 1996, **14**, 33 – 38.

59 G. Lukat, J. Krüger and B. Sommer, *J. Chem. Inf. Model.*, 2013, **53**, 2908 – 2925.

60 N. Michaud-Agrawal, E. J. Denning, T. B. Woolf and O. Beckstein, *J. Comput. Chem.*, 2011, **32**, 2319 – 2327.

61 D. Cheung, *Journal of Chemical Physics*, 2014, **141**, 194908.

62 S. Hu, C. Huang, H. Tsao and Y. Sheng, *Phys. Rev. E*, 2019, **99**, 012403.

63 L. V. Schäfer, D. H. de Jong, A. Holt, A. J. Rzepiela, A. H. de Vries, B. Poolman, J. A. Killian and S. J. Marrink, *Proc. Natl. Acad. Sci. U.S.A.*, 2011, **108**, 1343 – 1348.

64 D. L. Parton, J. W. Klingelhoefer and M. S. Sansom, *Biophys. J.*, 2011, **101**, 691 – 699.

65 J. J. Madsen, J. M. A. Grime, J. S. Rossman and G. A. Voth, *Proc. Natl. Acad. Sci. U.S.A.*, 2018, **115**, E8595 – E8603.

66 D. L. Parton, A. Tek, M. Baaden and M. S. P. Sansom, *PLoS Comput. Biol.*, 2013, **9**, e1003034.

67 O. H. Ollila, H. J. Risselada, M. Louhivouri, R. Lindahl, I. Vattulainen and S. J. Marrink, *Phys. Rev. Lett.*, 2009, **102**, 078101.

68 S. Yefimov, E. van der Giesson, P. R. Onck and S. J. Marrink, *Biophys. J.*, 2008, **94**, 2994 – 3002.

69 J. Yoo and Q. Cui, *Biophys. J.*, 2013, **104**, 128 – 138.

70 M. C. Heinrich, I. Levental, H. Gelman, P. A. Janmey and T. Baumgart, *J. Chem. Phys. B*, 2008, **112**, 8063–8068.

71 T. Baumgart, S. T. Hess and W. W. Webb, *Nature*, 2003, **23**, 821–824.

72 A. Tian, C. Johnson, W. Wang and T. Baumgart, *Phys. Rev. Lett*, 2007, **98**, 208102.

73 R. Lipowsky, *Journal de Physique II*, 1992, **2**, 1825–1840.

74 C. M. Rosetti, G. G. Montich and C. Pastorino, *J. Phys. Chem. B*, 2017, **121**, 1587–1600.

75 M. R. Rasch, E. Rossinyol, J. L. Hueso, B. W. Goodfellow and B. A. Korgel, *Nano. Lett*, 2010, **10**, 3733–3739.

76 Y. Guo, E. Terazzi, R. Seemann, J. B. Fleury and V. A. Baulin, *Science Advances*, 2016, **2**, e1600261.

77 S. Katira, *PhD thesis*, University of California, Berkeley, 2015.